



Valley-dependent tunneling through electrostatically created quantum dots in heterostructures of graphene with hexagonal boron nitride

A. Belayadi ^{1,2,*}, N. A. Hadadi,^{3,†} P. Vasilopoulos,^{4,‡} and A. Abbout ^{3,§}

¹*Ecole Supérieure des Sciences des Aliments et des Industries Alimentaires, ESSAIA, El Harrach, 16200 Algiers, Algeria*

²*University of Science and Technology Houari Boumediene, Bab Ezzouar, 16111 Algiers, Algeria*

³*Department of Physics, King Fahd University of Petroleum and Minerals, 31261 Dhahran, Saudi Arabia*

⁴*Department of Physics, Concordia University, 7141 Sherbrooke Ouest, Montréal, Québec H4B 1R6, Canada*



(Received 30 March 2023; accepted 26 June 2023; published 14 August 2023)

Kelvin probe force microscopy (KPFM) has been employed to probe charge carriers in a graphene/hexagonal boron nitride (hBN) heterostructure [*Nano Lett.* **21**, 5013 (2021)]. We propose an approach for operating valley filtering based on the KPFM-induced potential U_0 instead of using external or induced pseudomagnetic fields in strained graphene. Employing a tight-binding model, we investigate the parameters and rules leading to valley filtering in the presence of a graphene quantum dot (GQD) created by the KPFM tip. This model leads to a resolution of different transport channels in reciprocal space, where the electron transmission probability at each Dirac cone ($\mathbf{K}_1 = -\mathbf{K}$ and $\mathbf{K}_2 = +\mathbf{K}$) is evaluated separately. The results show that U_0 and the Fermi energy E_F control (or invert) the valley polarization, if electrons are allowed to flow through a given valley. The resulting valley filtering is allowed only if the signs of E_F and U_0 are the same. If they are different, the valley filtering is destroyed and might occur only at some resonant states affected by U_0 . Additionally, there are independent valley modes characterizing the conductance oscillations near the vicinity of the resonances, whose strength increases with U_0 and are similar to those occurring in resonant tunneling in quantum antidots and to the Fabry-Perot oscillations. Using KPFM, to probe the charge carriers, and graphene-based structures to control valley transport, provides an efficient way for attaining valley filtering without involving external or pseudomagnetic fields as in previous proposals.

DOI: [10.1103/PhysRevB.108.085419](https://doi.org/10.1103/PhysRevB.108.085419)

I. INTRODUCTION

Graphene-based materials are excellent candidates for spintronic applications. Indeed, the presence of one or several types of spin-orbit couplings (SOCs) [1–4] led to many experimental and theoretical studies of these materials in order to control spin-transport properties in ultrathin spintronic devices [5–7]. Besides potential use in spintronics, many recent applications have adopted graphene as an essential material to constitute unique (fundamental) platforms in valleytronics [8–10]. In this context, investigating valley filtering in graphene-based devices may facilitate the use of the valley degree of freedom in \mathbf{k} space, instead of the spin degree of freedom, as an alternative basis for future applications in valleytronics.

Valley filtering in graphene has been studied using quantum points contacts [11] as well as the departure from the usual linear E vs k dispersion adopted in most studies, referred to as trigonal warping [12,13]. To our knowledge though, there has been no experimental realization or confirmation of the predictions. For a comprehensive account of and different approaches to the subject, see the review [14].

Some valley-filtering proposals have used a graphene layer, with uniform zigzag edges, and stressed it in a particular way that leads to the emergence of pseudomagnetic fields (PMFs) [15–18]. It has also been shown that the valley-filtering process might occur in a honeycomb lattice that contains a line of heptagon-pentagon defects [19–21]. Further, recent scanning tunneling microscopy (STM) and Kelvin probe force microscopy (KPFM) experiments claimed that by breaking the potential symmetry in the substrates of graphene-based heterostructures, by applying real magnetic fields [4,22,23], the valley degeneracy might be lifted if some conditions are fulfilled. These conditions, discussed in Refs. [24–28], concern the KPFM tip potential, which electrostatically defines the GQDs, the presence or absence of a magnetic field, and the angle of incidence of the incoming electrons.

Very recently, a nanoscale valley splitting has been observed in confined states of graphene quantum dots. In this case, the presence of a magnetic field and an STM-induced potential, originating from the boron nitride substrate beneath the graphene layer, provide an alternative device for valleytronics [25–27,29]. However, in such cases the STM tip breaks the electron-hole symmetry and the magnetic field breaks the time-reversal symmetry; this will lead to an interplay between spintronics and valleytronics.

The question then arises whether an alternative way exists to lift the valley degeneracy without confinement, that traps electrons around the STM potential, and without lifting the spin degeneracy. Indeed, from an application point of view

*abelayadi@usthb.dz

†Onaif099@gmail.com

‡p.vasilopoulos@concordia.ca

§adel.abbout@kfupm.edu.sa

and for a better tunability of transport properties, one needs to avoid the confinement of the electrons by the STM-induced potential since they could tunnel through the induced potential barrier and contribute to the transmitted charge or valley current. Fortunately, several studies have shown that the presence of a magnetic field B along with the STM-induced potential do not always favor the confinement. For instance, in the case of a Gaussian shaped STM potential in a weak field B , electrons are more likely to escape into the induced potential barrier [24]. More precisely, in a weak field B with a circularly symmetric potential portrayed by a Gaussian model [22,24,27,30], the confinement leads to a compromise between the strengths of the potential and of the field B .

As current conservation between the source and the drain leads of the graphene flake is desired, a STM tip is not well suited for probing charge carriers since the current from the source reservoir will tunnel through the tip as well. We need an alternative method to create a graphene quantum dot (GQD) and keep the current conserved. Fortunately, KPFM has been recently adopted as an efficient method in which tunneling can be neglected [31]. In contrast to STM, KPFM can induce an electrostatic potential and form a GQD on a surface without the effects of local tip gating. Indeed, this is so because it is performed at slightly larger tip-sample distances, such that tunneling and van der Waals forces are significantly minimized [26,31].

Based on the arguments stated above and in order to better focus on valley polarization in graphene/hBN heterostructures with induced quantum dots, with the electron transmission probability accounted for \mathbf{K}_1 and \mathbf{K}_2 independently, it is strongly recommended to avoid both confinement and tunneling of electrons as well as lifting of the spin degeneracy caused by a magnetic field. Accordingly, we investigate valley-polarized transport in a graphene monolayer placed on top of a hBN substrate, with a voltage induced by a KPFM tip, in the absence of a magnetic field. Further motivation for our investigation comes from the experimental valley polarization in MoS₂ monolayers [32–34] and bismuth [35], valley transport in diamond [36], and the report of valley currents [37], and switches [9] in bilayer graphene. We hope the present paper will lead to a new way of experimentally investigating the valley degree of freedom using a KPFM tip.

The results are organized as follows. In Sec. II we describe the graphene/hBN heterostructure in the presence of a quantum dot created electrostatically by KPFM. We then use a tight-binding model to investigate valley-dependent transport. In Sec. III we present and discuss numerical results and in Sec. IV a summary.

II. MODEL AND METHODS

We consider a graphene/hBN heterostructure as shown in Fig. 1(a). A charge current at the graphene surface is controlled by the bias voltage V_B applied between the source (S) and drain (D) leads. The KPFM tip acts as a top gate V_T and tunes the potential, which induces an electric field that forms a stationary distribution [see Fig. 1(c)] of the charges on the hBN substrate [24,26,27]. To evaluate the resulting screened potential U several authors have solved the Poisson equation self-consistently assuming a KPFM-induced voltage pulse U_0

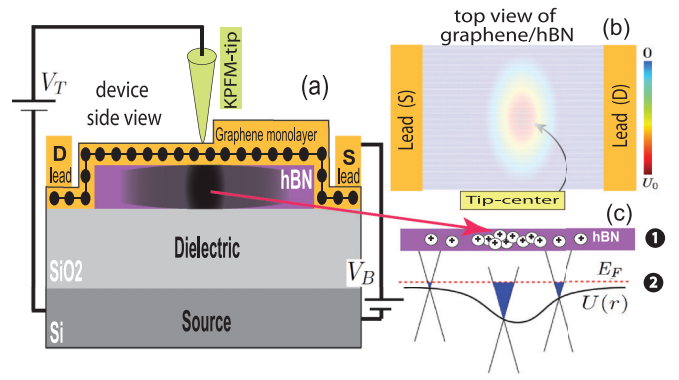


FIG. 1. Schematic of a device to operate valley filtering. In (a) we show the device, placed on top of a hBN substrate, made of a graphene sheet with zigzag boundaries. The insulating substrate defines the dielectric area such as SiO₂ and a back-gate substrate (source) as Si, for instance. In (b) we show the total screened potential felt by the graphene sheet due to the stationary charge distribution in line with experimental studies [26]. Panel (c) illustrates (1) the stationary distribution of the charges in the hBN substrate, due to the KPFM tip, and underneath it. (2) The sketch of the induced potential $U(r)$ and the Fermi energy E_F where we illustrate the position of the Dirac point for a given position r

and radius R_0 . At zero-magnetic field, the screened potential $U(r)$ is modeled by [24,26,27]

$$U(r_i) \simeq U_0 \exp(-r_i^2/R_0^2) + U_\infty, \quad (1)$$

where r_i is the discretized distance of the graphene sites i from the center of the KPFM tip. We denote by U_0 the electric potential at the center and R_0 its corresponding radius. The third term U_∞ defines the background value and can be controlled (cancelled out) by a back-gate voltage [26,27].

The model potential U , in Eq. (1), is used in a tight-binding Hamiltonian to investigate the valley transport properties in the presence of the tip-induced potential. We adopt a tight-binding model in a honeycomb lattice holding a single p_z orbital per site and neglect the chemical bonding or any modification in the atomic structure of graphene and hBN layers [38,39]. The resulting Hamiltonian that describes the system is given by

$$H = -t \sum_{(i,j)} \mathbf{a}_i^\dagger \mathbf{b}_j + \sum_{(i)} \Delta_{SG} (\mathbf{a}_i^\dagger \mathbf{a}_i - \mathbf{b}_i^\dagger \mathbf{b}_i) + \sum_{(i)} U_i (\mathbf{a}_i^\dagger \mathbf{a}_i + \mathbf{b}_i^\dagger \mathbf{b}_i), \quad (2)$$

where \mathbf{a}_i^\dagger (\mathbf{b}_i^\dagger) and \mathbf{a}_j (\mathbf{b}_j) are the creation and annihilation operators for an electron in graphene sublattice A (B) at sites i and j , respectively. The hopping energy is denoted by t and the on-site term is set to zero (Fermi level). The heterostructure introduces an additional second term Δ_{SG} , which describes the induced sublattice gap that arises mainly from the presence of the hBN substrate beneath the graphene layer [38,39].

Theory and experiments have been analyzed and compared in the presence of a STM or KPFM tip, and have shown that the screened potential $U(r)$ depends on the radius R_0 of the KPFM tip. For a Gaussian shape they have used the

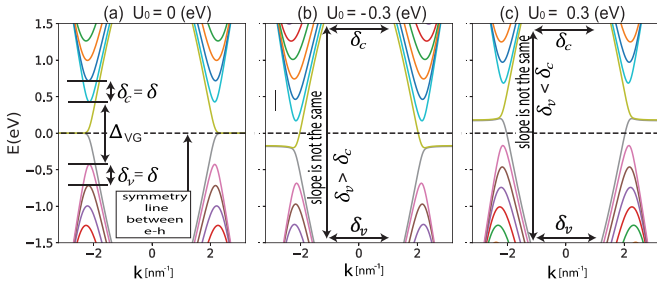


FIG. 2. Energy spectrum of a two-dimensional (2D) zigzagged strip 3 nm wide. Panel (a) shows the spectrum in the absence of a tip-induced potential ($U_0 = 0$). When the Fermi energy E_F is larger than $\Delta_{VG}/2$, where Δ_{VG} is the valley-mode spacing gap, the $-\mathbf{K}$ and $+\mathbf{K}$ channels are propagating. The valence and conduction mode spacings are denoted by δ_v and δ_c , respectively; Panels (b) and (c) show the spectrum in the presence of an induced potential with $U_0 = -0.3$ eV and $U_0 = +0.3$ eV, respectively. To see the effect of the broken e-h symmetry and compare (a), (b), and (c), we keep the dashed line at the reference energy $E_F = 0$. We indicate the difference in slope of the valence and conduction bands depending on the sign of U_0 for a given E_F : we have $v_v < v_c$ ($U_0 < 0$) or $v_v > v_c$ ($U_0 > 0$).

range $20 \text{ nm} < R_0 \leq 70 \text{ nm}$ [25,40–42]. Similarly, we will consider a graphene/hBN channel with zigzag edges, width $W = 110 \text{ nm}$, and length $L = 300 \text{ nm}$. Further, we take $t = -2.7 \text{ eV}$ and $\Delta_{SG} = 29.26 \text{ meV}$ [39,43,44], a tip radius $R_0 = 55 \text{ nm}$, and $U_\infty = 0$ since the value of U_∞ can be controlled by a gate voltage [26,27].

III. RESULTS AND DISCUSSION

Below we discuss how the Fermi energy E_F and the induced KPFM potential lead to valley filtering when only one valley channel is active and some conditions are fulfilled/ We compute the transmittance of each valley and show that the relevant conditions concern mainly the signs of E_F and U_0 and their ranges.

A. Electron-hole symmetry broken by the KPFM tip potential

Before stepping into the process of valley filtering and investigating the parameters that affect and monitor the valley transport in the presence of the induced electrostatic potential, we start by showing the dispersion relation for zigzag boundaries of the honeycomb lattice in Fig. 2. For operating valley filtering, it is important to have propagating modes at both valleys. This is achievable in a 2D zigzag strip, when E_F is higher than $|\Delta_{VG}/2|$, where Δ_{VG} is the valley-mode spacing gap, as shown in Fig. 2(a). For this reason, the valley-dependent conductances in the system can be addressed independently only beyond this limit defined by what we call the valley-mode gap Δ_{VG} with both the $-\mathbf{K}$ and $+\mathbf{K}$ channels propagating.

Additionally, it is clearly observed from the band spectrum in Figs. 2(b) and 2(c) that the electron-hole symmetry is broken by the induced potential, where the conduction and valence bands are not affected simultaneously by the same value of induced potential U_0 (nonvanishing value for the

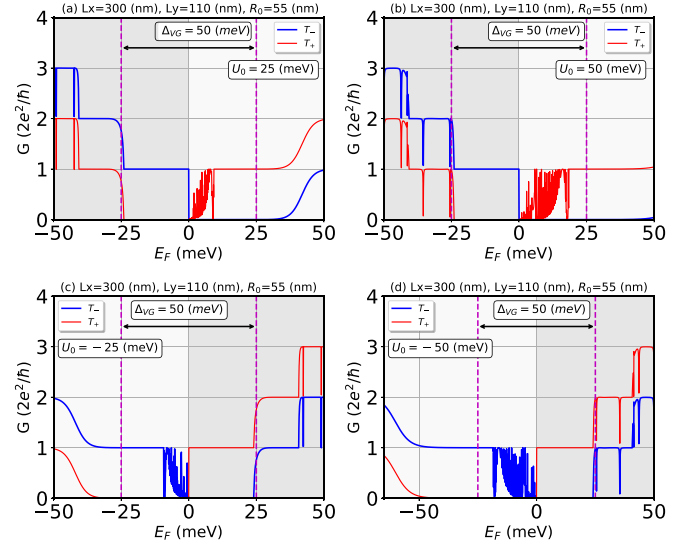


FIG. 3. Valley conductance vs Fermi energy for positive (top) and negative (bottom) induced potential U_0 as indicated. The red and dark blue curves show, respectively, the valley transmissions T_+ and T_- . Δ_{VG} is specified in the insets to all panels and the geometrical parameters on their tops.

potential at the border of the system due to the finite size of the system). In fact, positive values of the induced potential affect the quasiparticles for $E_F > 0$ while the negative ones affect them only for $E_F < 0$. The different behaviors of the quasiparticles at positive and negative E_F , caused by the induced potential, break the symmetry between the quasibound states in the valence and conduction bands and create the correct conditions for valley filtering of the propagating carriers at a given \mathbf{k} . As will be shown below, the Fermi velocity plays a major role in selecting the valley current

To resolve different transport channels in \mathbf{k} space, where the electron transmission probability of each Dirac cone is observed separately, we adopt the tight-binding model in Eq. (1), and we define the valley conductance G_- and G_+ related to the current flow across the induced potential at given Dirac cones $-\mathbf{K}$ and $+\mathbf{K}$, respectively. More details about computing valley conductance are discussed in Appendix A.

To investigate the dependence of the valley conductance in terms of the Fermi energy E_F and tip-induced potential pulse U_0 , we consider two cases: (1) the valley conductance is considered in terms of E_F for a fixed value of U_0 and (2) the valley conductance is considered in terms of U_0 for a fixed value of E_F .

B. Valley conductance in terms of the Fermi level

We have calculated the valley-dependent transmission at each valley independently for fixed tip potential $U_0 = \pm 25 \text{ meV}$ and $\pm 50 \text{ meV}$. The Fermi energy of the incident electrons varies between -50 meV and $+50 \text{ meV}$ and numerical results for the valley conductance, as a function of E_F , are shown in Fig. 3.

It is clear that by tuning the Fermi energy E_F one could operate a valley filter in a none symmetric energy range

and within the first propagating mode defined by the energy mode $E_m^{(1)}$. Depending on the sign of the induced potential and within an energy range, only one valley channel is allowed to pass. According to Fig. 3, the valley filtering happens when E_F is increased beyond the energy limit $\Delta_{VG}/2$. We find that, for positive values of the induced potential, as shown in Figs. 3(a) and 3(b), only one valley is allowed within the energy range $\Delta_{VG}/2 < E_F < E_m^{(1)}$ meV with $E_m^{(1)} = 30$ meV (50 meV) for $U_0 = 25$ meV (50 meV). We observe that 100%(0%) of the conductance results from the flow of electrons at $+\mathbf{K}$ ($-\mathbf{K}$) for positive E_F , while 50% of the conductance results from the flow of electrons at both valleys for negative $E_F < -\Delta_{VG}/2$.

The presence of the electrostatic potential induced from the KPFM tip does affect the quasibound states in the valence or conduction bands depending on the bias sign, as shown in Figs. 2(b) and 2(c). Consequently, the propagating modes of the electron quasiparticles (at positive energy) and hole quasiparticles (at negative energy) behave differently. As a result, valley-dependent transport, when the electron-hole symmetry is broken, will depend on the sign of E_F and U_0 . For instance, for $U_0 > 0$, at positive E_F the propagating modes are affected by the induced potential, and valley-dependent transmission occurs $E_F > \Delta_{VG}/2$. However, at negative E_F the propagating modes shift from the conduction to the valence bands, as shown in Fig. 2(c). This interband transition is not affected by the induced potential when U_0 is positive, and hence no valley-dependent transmission occurs at $E_F < -\Delta_{VG}/2$. Similarly, for negative induced potential, the electron propagating modes belonging to the conduction bands are not affected while the quasibound states in the valence bands are. Summarizing, valley filtering happens at $E_F < -\Delta_{VG}/2$ and destroyed at $E_F > \Delta_{VG}/2$.

On the basis of the above arguments, a valley-dependent transmission, i.e., a selective population of a single valley, is pronounced depending on the sign of U_0 and E_F . In more detail, we contrast the slopes in the dispersion relations of the valence and conduction bands according to the signs of E_F and the induced potential. This contrast does explain the presence (absence) of valley filtering at $E_F > |\Delta_{VG}/2|$ for positive (negative) values of U_0 . More precisely, for a given E_F this slope does affect the Fermi velocities depending on the sign of U_0 as shown in Fig. 2. To confirm this assertion, we refer again to the dispersion relation, for zigzag boundaries, where we express the Fermi velocity in terms of the mode spacing δ or band gap Δ_{VG} as [11]

$$\Delta_{VG} = \sqrt{3}\pi ta/2W = \pi \hbar v/W \quad (3)$$

where $v = (\sqrt{3}/2)ta/\hbar = 3 \times 10^6$ m/s is the Fermi velocity in pristine graphene. In our case, with the tight-binding parameters and sample shapes specified in Sec. II, we have $\Delta_{VG} = 50$ meV, where $\delta_v = \delta_c = \Delta_{VG}/3 = \pi \hbar v/3W$. Hence, the mode spacing is straightforwardly derived from the velocity and vice versa.

One important remark that we might also highlight from the output of Fig. 3 is the presence of an oscillatory behavior that is valley dependent. Indeed, the oscillations near the vicinity of the mode opening energy is appearing due to the potential in the scattering region, where only few mode

(valley dependence) are affected by the potential landscape of the GQDs and behave similarly to the Fabry-Perot oscillation [45]. More precisely, the conductance oscillations are valley dependent and many features of conductance oscillations are similar to the resonant tunneling in quantum antidots [46,47]. Importantly, as shown in Fig. 3, \mathbf{K}_1 (\mathbf{K}_2) valley modes are affected by tip-potential landscape and feature conductance oscillations at negative (positive) Fermi levels where the resonance increases proportionally with induced potential and happens only within the valley-mode gap when both E_F and U_0 have the same polarity.

Figure 3 shows a clear asymmetry between the two valleys. Indeed, the presence of an additional edge state mode for one valley only explains the extra quantum of conductance in the profile of the valley conductance. The other source of the asymmetry is the tip-induced potential: The Fermi velocity, at positive or negative incident energy *relative to the tip-induced potential*, is no longer the same and becomes a function of U_0 (the potential decays toward the leads). For this reason, based on the band curvature and Fermi velocity a valley mode is allowed only if the signs of E_F and U_0 are the same.

C. Valley conductance in terms of the induced potential

When a tip potential is induced, the Fermi velocity, at positive or negative incident energy around the tip-induced potential is no longer the same and becomes a function of U_0 . Indeed, The presence of the contacts (left and right reservoirs) makes the system finite and therefore the tip's induced potential does not vanish near the leads. One has to consider that reminiscent component of the potential in the lead and thus ends up with a band structure with different Fermi velocities (v_c, v_v) at the conduction and valence bands.

We bear in mind that the Fermi wavelength λ_F is inversely proportional to the Fermi velocity v_F . The conductance is very sensitive to the variation of λ_F (especially for large quantum dots). In fact, far from the modes opening, the Fermi velocity approaches that of infinite pristine graphene and therefore it barely varies. In contrast, near the mode opening, where the band is highly nonlinear, the Fermi velocity varies a lot with E_F and this explains why depending on the sign of ($U_0 \times E_F$), $\lambda_F^{-K} \neq \lambda_F^{+K}$ and therefore, as we can deduce from the band structure, the filtering can happen or not.

Now let us go back to Fig. 3 and discuss the range of valley filtering. It is seen that by increasing the value of the induced potential U_0 from 25 meV to 50 meV, the energy range of the valley filtering increases since the energy mode is sensitive to the value of U_0 ($E_m^{(1)} \propto U_0$) and steps from 30 meV to 50 meV, respectively. From Figs. 2 and 3, we infer that for positive U_0 and E_F , the electron propagating modes are strongly affected and the energy mode $E_m^{(1)}(U_0 = 25 \text{ meV}) \neq E_m^{(1)}(U_0 = 50 \text{ meV})$ where the conductance exhibits a smooth less quantized plateaus. For negative E_F the modes are not affected by U_0 where $E_m^{(1)}(U_0 = 25 \text{ meV}) = E_m^{(1)}(U_0 = 50 \text{ meV})$, and hence the conductance exhibits quantized plateaux at an odd number of $2e^2/\hbar$ where 2 stands for spin degeneracy. However, for negative induced potential, the process is entirely inverted because for negative E_F the propagating

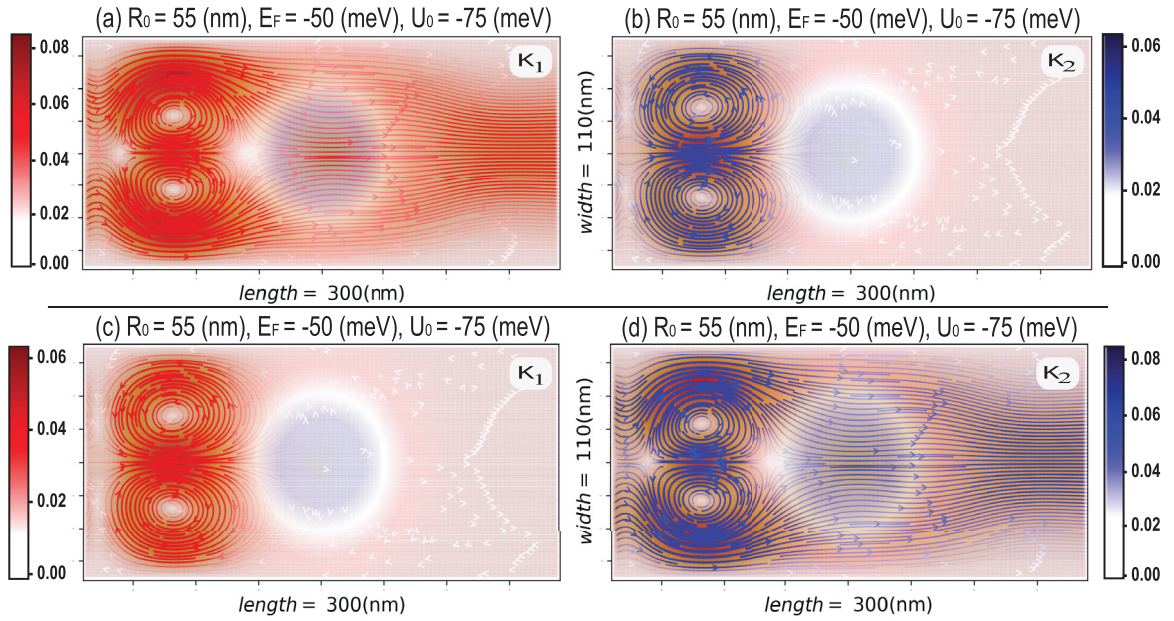


FIG. 4. Real-space mapping of both valley currents [red (blue) lines show the $\mathbf{K}_1 = -\mathbf{K}$ ($\mathbf{K}_2 = +\mathbf{K}$) current] in the presence of the induced potential U_0 . Panels (a) and (b) are for negative energy, while (c) and (d) are for positive energy. The sign of U_0 is set the same as that of E_F . The induced potential of the KPFM tip traps the charge in the hBN space and its effect (based on the Poisson equation) is illustrated by the spherical shape in the middle of the graphene sample [see map in Fig. 1(b)] held a few nanometers from the surface of graphene; it decays to zero for $(x^2 + y^2)^{1/2} > R_0$.

modes are strongly affected whereas for positive E_F they are not.

D. Rules for operating selective valley current

The analysis of Secs. III A and III B showed that valley filtering is allowed only when the sign of the product ($E_F \times U_0$) is positive. Indeed, beyond the valley-mode spacing gap ($E_F > \Delta_{VG}$) in Fig. 3, we showed that a positive (light-gray background) product leads to valley filtering of the current while a negative one (dark-gray background) destroys the valley filtering process. This is also shown in Fig. 4, where we plot the valley current in terms of E_F and U_0 and maintain the product $E_F \times U_0$ positive.

In more detail, we set the sign of U_0 the same as E_F and then select a positive (negative) value of E_F between $\Delta_{VG}/2$ ($-\Delta_{VG}/2$) and $E_m^{(1)}$ ($-E_m^{(1)}$), cf. Fig. 3. Once these conditions are fulfilled, we map the current of the propagating channel at $\mathbf{K}_1 = -\mathbf{K}$ and $\mathbf{K}_2 = +\mathbf{K}$. The corresponding current is evaluated and mapped in Fig. 4.

As illustrated in Fig. 4, the valley filtering process is operative due to the positive sign of the product $E_F \times U_0$. Interestingly, the currents for both positive and negative E_F are equal, but the opposite energy sign shifts the valleys with only one valley allowing current to flow and the other one blocking it. Hence, depending on E_F and U_0 , one can break the valley degeneracy and generate a valley-polarized current. This is an important result as it leads to valley selection by changing either U_0 or a bias gate, which shifts E_F or changes its sign.

Below we will show that the valley filtering can also take place for some potentials and either sign of the product $E_F \times U_0$. This valley filtering does correspond to resonances with some states affected by the induced potential.

E. Valley filtering and resonances

As mentioned above, the tip-induced potential $U(r)$ breaks the symmetry between the valence ($E_F < 0$) and conduction ($E_F > 0$) bands and the valley-polarized conduction becomes sensitive to its sign and strength for a given $E_F > 0$. In Figs. 5(a) and 5(b) we show the conductance as a function of U_0 .

First, as in Sec. III B, the results show that the valley filtering depends on the sign of the product $E_F \times U_0$, which is the key point for breaking the valley degeneracy and creating a valley-polarized current. For instance, for $E_F \times U_0 > 0$ and at $E_F = -30$ meV, the conductance is polarized for U_0 in the

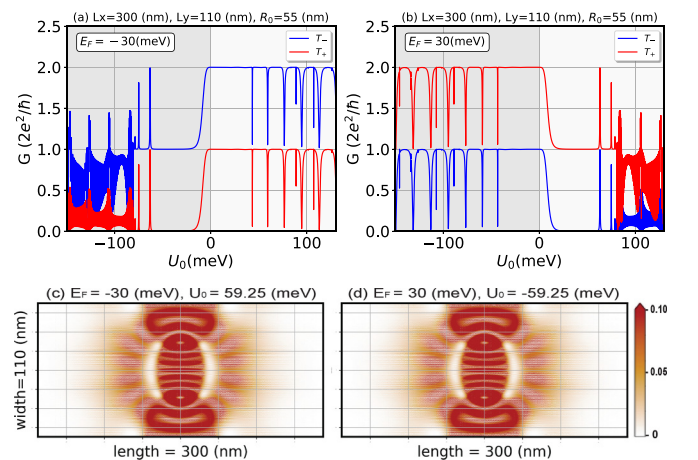


FIG. 5. Valley conductance vs tip-induced potential for negative (a) positive (b) Fermi level E_F . Panels (c) and (d) show the corresponding local density of resonant states. U_0 and E_F have opposite signs.

range $-60 \text{ meV} < U_0 < -\Delta_{VG}/2$ with only the $\mathbf{K}_1 = -\mathbf{K}$ channel conducting. However, for $E_F = +30 \text{ meV}$ the valley-selecting process is reversed and only the $\mathbf{K}_2 = +\mathbf{K}$ channel is conducting for U_0 in the range $-\Delta_{VG}/2 < U_0 < +60 \text{ meV}$.

Second, for $E_F \times U_0 < 0$ the obtained results show valley antiresonances (and resonances) where the conductance drops to zero with respect to valley conductance at only one Dirac cone (K_1 or K_2). This process can be justified due to valley confinement, [26,48,49]. In fact, quasibound states have been observed in Klein QDs, KQD being/called the region in which these quasibound states are localized. In our case such a confinement can be more precisely explained by the interference between the wave functions of the reflected and incident electrons that results in the formation of standing waves. In fact, a similar confinement has also been observed in graphene nanoribbons with an inhomogeneous out-of-plane Gaussian deformation of the strain with circularly symmetric geometry [15], where an enhancement of the density of states occurs in the strained region and leads to a decrease in the conductance.

In our case we have more insight into the confined states since we can distinguish the wave function by its valley index. This allows us to investigate valley signatures of transport in confined geometries, where we observe that the enhancement of the LDOS in the GQD region is valley dependent and accompanied by a decrease or increase in the conductance, signaling the presence or absence of a valley current.

More precisely, to show the presence of confined states we employ the kernel polynomial method (KPM) to numerically compute the local density of states (LDOS) using Chebyshev polynomials [50,51] along with damping kernels [50] as recently provided by a Pybinding package [52]. To compute the LDOS we count the sites contained within the shape of the induced potential, determined by $(x^2 + y^2)^{1/2} < R_0$. We observe that the electrons are almost localized at induced potential landscape, where the superposition of the confined states give rise to features of vortex pattern, which does appear at the induced potential boundaries.

The same remarks as in Fig. 4, can be drawn from Figs. 5(c) and 5(d) where the LDOS for $\mathbf{K}_1 = -\mathbf{K}$ and $\mathbf{K}_2 = +\mathbf{K}$ are equal, where the opposite energy sign shifts only the valleys with only one valley confined. Hence, depending on E_F and U_0 , one can break the valley degeneracy and generate valley confined states when the product $E_F \times U_0$ is negative.

The resonance at $U_0 = +59.25 \text{ meV}$ ($U_0 = -59.25 \text{ meV}$) occurs for negative (positive) E_F and results from confined states of the quasibands in the valence (conduction) band.

The main point here is that we confirm and show that the states in the case $U_0 = +59.25 \text{ meV}$ ($U_0 = -59.25 \text{ meV}$) are indeed resonant states with a high local density within the area that defines the GQDs. In our case, the interference might happen inside the induced island due to the shape of GQDs with specific values of induced potential.

Since we are dealing with electron-hole broken symmetry, positive and negative energy bands are affected independently by the induced potential. Also, since the ribbon width W is finite, the momentum is discretized. Therefore, the antiresonances for $E_F \times U_0 < 0$ [dark-gray area in Figs. 5(a) and 5(b)], can be clearly identified and appear nearly periodic. Since E_F does affect the set of discrete values in momentum

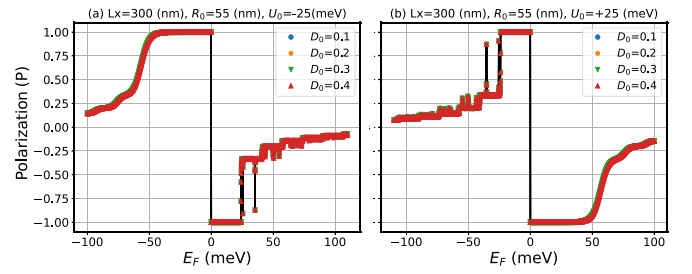


FIG. 6. Polarization vs Fermi energy for (a) negative and (b) positive induced potential.

space, we can state that different values of E_F lead to a different set of resonances with their number depending on the values of E_F and W .

F. Robustness of valley filtering against disorder and strip width

Operating valley filtering controlled by either U_0 or E_F must be robust against a disorder potential. For this purpose, in Fig. 6, the valley polarization is plotted as a function of E_F in the presence of an on-site disorder of strengths D_i . The relevant Hamiltonian is $H_D = H + \sum_{(i)} D_i (\mathbf{a}_i^\dagger \mathbf{a}_i + \mathbf{b}_i^\dagger \mathbf{b}_i)$, where H is defined in Eq. (2) and D_i are numbers randomly distributed in the range $[-D_0, +D_0]$. We will consider a strong disorder $5U_0 < D_0 < 15U_0$. We notice that the disorder does not affect the polarization even for values stronger than $D_0 = 15U_0$. For all considered disorder strengths, Fig. 6 shows that a valley filtering is always present and robust against on-site disorder.

Additionally, we have also considered the effect of the ribbon width and plotted, in Fig. 7, the valley conductance versus E_F for several widths W , determined by the ratio $r = W/R_0$, for a Gaussian shape with $R_0 = 35 \text{ nm}$. We focus on the side on which $E_F \times U_0 > 0$ and valley filtering operates

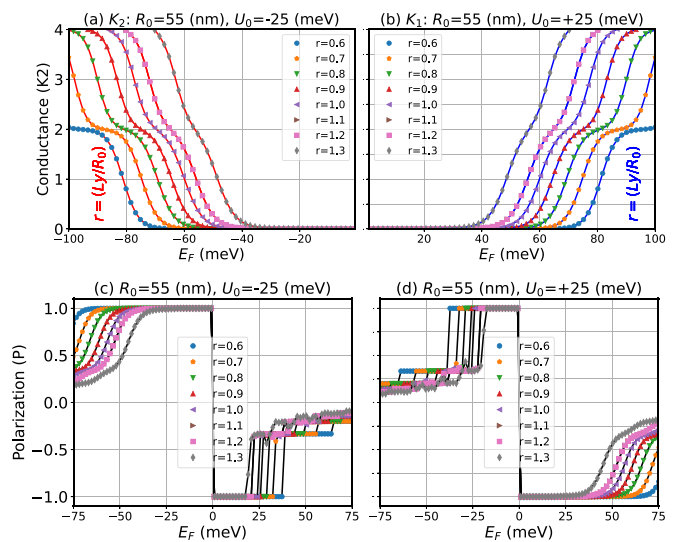


FIG. 7. The top panels show the valley conductance, at K_2 in (a) and at K_1 in (b), vs E_F for several widths W determined by $r = W/R_0$. The bottom panels show the polarization vs E_F for several values r .

as discussed previously. We notice that the valley filtering is more evident for $r \leq 1$. More precisely, for $r = 0.6, 0.7, 0.8$, we have, respectively, the energy ranges $-0.72 \leq E \leq +0.72$, $-0.64 \leq E \leq +0.64$, and $-0.58 \leq E \leq +0.58$ meV, where the $+$ ($-$) signs are for $U_0 = +25$ meV ($U_0 = -25$ meV), respectively. From Figs. 7(a) and 7(b), we can see that the conductance plateaux are flatter for $r < 1$ than for $r > 1$. Additionally, from Figs. 7(c) and 7(d) we clearly observe that by increasing the ratio r the energy range of controlling the valley filtering decreases and it might vanish for $r > 1$ since E_F falls between 0 and $\Delta_{VG}/2$. More precisely, for $r > 1$ the polarization drops and we have $P < |1|$ for $E_F > |\Delta_{VG}/2|$.

Regarding the sample shape, what matters most is not the width W of the sample, but the ratio $r = W/R_0$. If R_0 is much smaller than W , the valley filtering will be destroyed since the electrons will be scattered from the sample edge and will not feel the screened potential; then both valleys contribute to the current. For this reason valley filtering is destroyed as discussed in Fig. 7. Additionally, the choice of W also matters since it is very important to keep the range of E_F within a few meV. That is, we avoid using a narrow width and consider only the case $W \gg a$ so that the mode spacing gap is a few meV wide as specified after Eq. (3).

IV. SUMMARY AND CONCLUSIONS

We presented an approach for operating valley filtering based on the KPFM-induced potential that opens various roads to experimental verification. Using such an electrostatic potential, instead of PMFs induced from nanobubbles, we can operate or destroy the valleys filtering depending on the signs of the electron energies and the induced potential. A positive sign of their product ($U_0 \times E_F > 0$) allows operating valley filtering, and the bias voltage, which controls the energy sign, shifts the valleys *with only one of them allowing current to flow and the other one being blocked*.

We have also noticed the presence of conductance oscillations near the vicinity the mode opening energy, which are valley dependent and whose strength is proportional to that of the induced potential within the mode-spacing gap. These oscillations are similar to those in resonant tunneling in quantum antidots and to the Fabry-Perot ones. Furthermore, valley polarized currents can occur for negative products $U_0 \times E_F < 0$. In such a case the valley filtering does correspond to resonances; some states are affected by the induced potential and only propagating states belonging to one valley confined in the induced QDs occur.

The proposed contribution suggests an alternative way to experimentally realize valley-polarized currents in electrostatically created quantum dots on graphene/hBN heterostructures. Within this framework, the induced potential together with the sign and the range of the incident electron energies directly affect the behavior of the setup. With these factors in mind, one can conveniently exploit both valley confinement and valley filtering in devices where the simulation discloses possible functionalities within a few meV of energy range.

To sum up, we find that valley is controlled by the sign of $U_0 \times E_F$. The results of the present study simply provide

an alternative approach, that can facilitate the development of valleytronic devices. For other possible ways to achieve valley filtering, we refer to the review [14].

ACKNOWLEDGMENTS

The authors acknowledge computing time on the SHAH-HEN supercomputers at KAUST University.

APPENDIX A: VALLEY-DEPENDENT TRANSMISSION AND POLARIZATION

Below we briefly describe the derivation of the valley-dependent transmittance and polarization expressions. The propagating modes in the leads can be selected depending on their velocity and momentum direction [53,54]. This is achieved using the Kwant functionalities [55] that couple the propagating modes with the scattering region and therefore allow the evaluation of valley transport properties. We consider only propagating modes and assume that valley modes are defined based on propagating states $\Phi(\mathbf{v} < \mathbf{0})$ [55]. These states are characterized by both degrees that contain the two valleys \mathbf{K}_1 [obtained from $\Phi(\mathbf{k} < \mathbf{0}, \mathbf{v} < \mathbf{0})$] and \mathbf{K}_2 [obtained from $\Phi(\mathbf{k} > \mathbf{0}, \mathbf{v} < \mathbf{0})$] in the graphene lead [18]. Once the valley states are defined, we resolve different transport channels in reciprocal space, with the electron transmission probability at each Dirac cone computed separately. Within the Green's function approach [56,57] the valley-resolved channels lead to the total transmittance of electrons $T = T_{-K} + T_{+K}$, where the valley transmittance $T_{\pm K}$ given by

$$T_{\pm K}^{m,n} = \text{Trace}[G_{\pm K} \Gamma^m G_{\pm K}^\dagger \Gamma^n], \quad (m, n = L, R). \quad (\text{A1})$$

The Green's function matrices are given by

$$G(\epsilon, \pm \mathbf{K}) = [(\epsilon + i\eta)I - H^h(\pm \mathbf{K}) - \Sigma]^{-1} \quad (\text{A2})$$

and

$$\Gamma = i(\Sigma - \Sigma^\dagger). \quad (\text{A3})$$

Γ is the imaginary part of the self-energy of the contact given by coupling, independently, the scattering region (defined by the Hamiltonian H^h) with each valley mode. For more details see Refs. [18,58]. Once the valley-dependent transmission is derived, we define the valley conductance G_- and G_+ at the Dirac cones $-\mathbf{K}$ and $+\mathbf{K}$, respectively as $G_{\pm} = (e^2/h)T_{\pm K}$. To obtain both valley modes and ensure valley-resolved channels, we consider the propagating modes for $E_F > \text{abs}(\Delta_{VG}/2)$ (cf, Fig. 2). After obtaining them the two valleys can be separated depending on their momentum sign. The resulting valley polarization is obtained as

$$P = \frac{T_{-K} - T_{+K}}{T_{-K} + T_{+K}}. \quad (\text{A4})$$

For $P = \pm 1$ the electrons are localized entirely at the $\pm \mathbf{K}$ valley and full polarized transmittance is ensured. $P = 0$ corresponds to unpolarized electrons.

We might also obtain the local density of states (LDOS) at a given sample site i as

$$\text{LDOS}(E) = \sum_l | \langle i|l \rangle |^2 \delta(E - E_l), \quad (\text{A5})$$

the energy E is the energy of the confined states where the summation is over all electron eigenstates $|l\rangle = c_l^\dagger|0\rangle$ of the Hamiltonian H in Eq. (2) with energy E_l . The quantity in Eq. (A5) is numerically computed using Chebyshev polynomials [50,51] and damping kernels [50].

APPENDIX B: VALLEY CURRENT MAPPING

We adopt the procedure detailed in the Kwant package [55]. The density operator and continuity equation are expressed as

$$\rho_q = \sum_a \Phi_a^* H_q^h \Phi_a, \quad \frac{\partial \rho_a}{\partial t} - \sum_b J_{a,b} = 0. \quad (\text{B1})$$

H^h is the Hamiltonian of the heterostructure in the scattering region whose size is $N_1 \times N_2$ sites and $\Phi(\mathbf{v} < \mathbf{0})$ is the eigenstate of the propagating mode of the graphene's lead whose size is N_1 . Here q defines all

sites or hoppings in the scattering region and J_{ab} is the current.

For a given site of density ρ_a , we sum over its neighboring sites b . Then the valley current $J_{\pm\mathbf{k}}^{ab}$ takes the form

$$J_{-\mathbf{k}}^{ab} = \Phi^*(\mathbf{k} < \mathbf{0}, \mathbf{v} < \mathbf{0}) \left(i \sum_\gamma H_{ab\gamma}^{*h} H_{a\gamma}^h - H_{a\gamma}^h H_{ab\gamma} \right) \times \Phi(\mathbf{k} < \mathbf{0}, \mathbf{v} < \mathbf{0}), \quad (\text{B2})$$

and

$$J_{+\mathbf{k}}^{ab} = \Phi^*(\mathbf{k} > \mathbf{0}, \mathbf{v} < \mathbf{0}) \left(i \sum_\gamma H_{ab\gamma}^{*h} H_{a\gamma}^h - H_{a\gamma}^h H_{ab\gamma} \right) \times \Phi(\mathbf{k} > \mathbf{0}, \mathbf{v} < \mathbf{0}), \quad (\text{B3})$$

where H_{ab} is a matrix with zero elements except for those connecting the sites a and b . In this case, the hopping matrices in the heterostructure are obtained from the first term of Eq. (2).

-
- [1] F. Herling, C. K. Safeer, J. Ingla-Aynés, N. Ontoso, L. E. Hueso, and F. Casanova, Gate tunability of highly efficient spin-to-charge conversion by spin Hall effect in graphene proximitized with WSe₂, *APL Mater.* **8**, 071103 (2020).
- [2] W. S. Torres, J. F. Sierra, L. A. Benítez, F. Bonell, J. H. García, S. Roche, and S. O. Valenzuela, Magnetism, spin dynamics, and quantum transport in two-dimensional systems, *MRS Bull.* **45**, 357 (2020).
- [3] K. Zollner, A. W. Cummings, S. Roche, and J. Fabian, Graphene on two-dimensional hexagonal BN, AlN, and GaN: Electronic, spin-orbit, and spin relaxation properties, *Phys. Rev. B* **103**, 075129 (2021).
- [4] Z. Fan, J. H. Garcia, A. W. Cummings, J. E. Barrios-Vargas, M. Panhans, A. Harju, and S. Roche, Linear scaling quantum transport methodologies, *Phys. Rep.* **903**, 1 (2021).
- [5] J. F. Sierra, J. Fabian, R. K. Kawakami, S. Roche, and S. O. Valenzuela, van der Waals heterostructures for spintronics and opto-spintronics, *Nat. Nanotechnol.* **16**, 856 (2021).
- [6] A. Belayadi and P. Vasilopoulos, A spin modulating device, tuned by the Fermi energy, in honeycomb-like substrates periodically stubbed with transition-metal-dichalkogenides, *Nanotechnology* **34**, 085704 (2023).
- [7] A. Belayadi and P. Vasilopoulos, Spin-dependent polarization and quantum Hall conductivity in decorated graphene: Influence of locally induced spin-orbit-couplings and impurities, *Nanotechnology* **34**, 365706 (2023).
- [8] L. L. Tao and E. Y. Tsymlal, Two-dimensional spin-valley locking spin valve, *Phys. Rev. B* **100**, 161110 (2019).
- [9] Y. W. Liu, Z. Hou, S. Y. Li, Q. F. Sun, and L. He, Movable Valley Switch Driven by Berry Phase in Bilayer-Graphene Resonators, *Phys. Rev. Lett.* **124**, 166801 (2020).
- [10] D. Zambrano, P. A. Orellana, L. Rosales, and A. Latgé, Spin and Valley Filter Based on Two-Dimensional WSe₂ Heterostructures, *Phys. Rev. Appl.* **15**, 034069 (2021).
- [11] A. Rycerz, J. Tworzyno, and C. W. J. Beenakker, Valley filter and valley valve in graphene, *Nat. Phys.* **3**, 172 (2007).
- [12] J. M. Pereira, F. M. Peeters, Costa R. N. Filho, and G. A. Farias, Valley polarization due to trigonal warping on tunneling electrons in graphene, *J. Phys.: Condens. Matter* **21**, 045301 (2008).
- [13] J. L. Garcia-Pomar, A. Cortijo, and M. Nieto-Vesperinas, Fully Valley-Polarized Electron Beams in Graphene, *Phys. Rev. Lett.* **100**, 236801 (2008).
- [14] S. A. Vitale, D. Nezich, J. O. Varghese, P. Kim, N. Gedik, P. Jarillo-Herrero, D. Xiao, and M. Rothschild, Valleytronics: Opportunities, challenges, and paths forward, *Small* **14**, 1801483 (2018).
- [15] R. Carrillo-Bastos, D. Faria, A. Latgé, F. Mireles, and N. Sandler, Gaussian deformations in graphene ribbons: Flowers and confinement, *Phys. Rev. B* **90**, 041411 (2014).
- [16] R. Carrillo-Bastos, C. León, D. Faria, A. Latgé, E. Y. Andrei, and N. Sandler, Strained fold-assisted transport in graphene systems, *Phys. Rev. B* **94**, 125422 (2016).
- [17] D. Faria, C. León, L. R. F. Lima, A. Latgé, and N. Sandler, Valley polarization braiding in strained graphene, *Phys. Rev. B* **101**, 081410 (2020).
- [18] T. Stegmann and N. Szpak, Current splitting and valley polarization in elastically deformed graphene, *2D Mater.* **6**, 015024 (2018).
- [19] D. Gunlycke and C. T. White, Graphene Valley Filter Using a Line Defect, *Phys. Rev. Lett.* **106**, 136806 (2011).
- [20] D. Gunlycke and C. T. White, Valley and spin polarization from graphene line defect scattering, *J. Vac. Sci. Technol. B* **30**, 03D112 (2012).
- [21] Y. Liu, J. Song, Y. Li, Y. Liu, and Q. F. Sun, Controllable valley polarization using graphene multiple topological line defects, *Phys. Rev. B* **87**, 195445 (2013).
- [22] G. Giavaras and F. Nori, Tunable quantum dots in monolayer graphene, *Phys. Rev. B* **85**, 165446 (2012).
- [23] L. A. Chizhova, F. Libisch, and J. Burgdörfer, Graphene quantum dot on boron nitride: Dirac cone replica and Hofstadter butterfly, *Phys. Rev. B* **90**, 165404 (2014).

- [24] A. Orlof, A. A. Shylau, and I. V. Zozoulenko, Electron-electron interactions in graphene field-induced quantum dots in a high magnetic field, *Phys. Rev. B* **92**, 075431 (2015).
- [25] N. M. Freitag, L. A. Chizhova, P. Nemes-Incze, C. R. Woods, R. V. Gorbachev, Y. Cao, and M. Morgenstern, Electrostatically confined monolayer graphene quantum dots with orbital and valley splittings, *Nano Lett.* **16**, 5798 (2016).
- [26] W. A. Behn, Z. J. Krebs, K. J. Smith, K. Watanabe, T. Taniguchi, and V. W. Brar, Measuring and tuning the potential landscape of electrostatically defined quantum dots in graphene, *Nano Lett.* **21**, 5013 (2021).
- [27] S. Y. Li and L. He, Recent progresses of quantum confinement in graphene quantum dots, *Front. Phys.* **17**, 33201 (2022).
- [28] M. I. Katsnelson, K. S. Novoselov, and A. K. Geim, Chiral tunnelling and the Klein paradox in graphene, *Nat. Phys.* **2**, 620 (2006).
- [29] S. Y. Li, Y. Su, Y. N. Ren, and L. He, Valley Polarization and Inversion in Strained Graphene via Pseudo-Landau Levels, Valley Splitting of Real Landau Levels, and Confined States, *Phys. Rev. Lett.* **124**, 106802 (2020).
- [30] P. A. Maksym and H. Aoki, Magnetic-field-controlled vacuum charge in graphene quantum dots with a mass gap, *Phys. Rev. B* **88**, 081406 (2013).
- [31] S. Samaddar, J. Coraux, S. C. Martin, B. Grévin, H. Courtois, and C. B. Winkelmann, Equal variations of the Fermi level and work function in graphene at the nanoscale, *Nanoscale* **8**, 15162 (2016).
- [32] T. Cao, G. Wang, W. Han, H. Ye, C. Zhu, J. Shi, and J. Feng, Valley-selective circular dichroism of monolayer molybdenum disulphide, *Nat. Commun.* **3**, 887 (2012).
- [33] H. Zeng, J. Dai, W. Yao, D. Xiao, and X. Cui, Valley polarization in MoS₂ monolayers by optical pumping, *Nat. Nanotechnol.* **7**, 490 (2012).
- [34] K. F. Mak, K. He, J. Shan, and T. F. Heinz, Control of valley polarization in monolayer MoS₂ by optical helicity, *Nat. Nanotechnol.* **7**, 494 (2012).
- [35] Z. Zhu, A. Collaudin, B. Fauqué, W. Kang, and K. Behnia, Field-induced polarization of Dirac valleys in bismuth, *Nat. Phys.* **8**, 89 (2012).
- [36] J. Isberg, M. Gabrysch, J. Hammersberg, S. Majdi, K. K. Kovi and D. J. Twitchen, Generation, transport and detection of valley-polarized electrons in diamond, *Nat. Mater.* **12**, 760 (2013).
- [37] Y. Shimazaki, M. Yamamoto, I. V. Borzenets, K. Watanabe, T. Taniguchi, and S. Tarucha, Generation and detection of pure valley current by electrically induced Berry curvature in bilayer graphene, *Nat. Phys.* **11**, 1032 (2015).
- [38] J. M. Marmolejo-Tejada, J. H. Garcia, M. D. Petrović, P. H. Chang, X. L. Sheng, A. Cresti, and B. K. Nikolić, Deciphering the origin of nonlocal resistance in multiterminal graphene on hexagonal-boron-nitride with *ab initio* quantum transport: Fermi surface edge currents rather than Fermi sea topological valley currents, *J. Phys.: Mater.* **1**, 015006 (2018).
- [39] G. Giovannetti, P. A. Khomyakov, G. Brocks, P. J. Kelly, and J. Van Den Brink, Substrate-induced band gap in graphene on hexagonal boron nitride: *Ab initio* density functional calculations, *Phys. Rev. B* **76**, 073103 (2007).
- [40] P. A. Maksym, M. Roy, M. F. Craciun, S. Russo, M. Yamamoto, S. Tarucha, and H. Aoki, Proposal for a magnetic field induced graphene dot, *J. Phys.: Conf. Ser.* **245**, 012030 (2010).
- [41] J. Lee, D. Wong, J. Velasco Jr., J. F. Rodriguez-Nieva, S. Kahn, H. Z. Tsai, T. Taniguchi, K. Watanabe, A. Zettl, F. Wang *et al.*, Imaging electrostatically confined Dirac fermions in graphene quantum dots, *Nat. Phys.* **12**, 1032 (2016).
- [42] H. V. Grushevskaya, G. G. Krylov, S. P. Kruchinin, and B. Vlahovic, Graphene quantum dots, graphene non-circular n-p-n-junctions: Quasi-relativistic pseudo wave and potentials, in *Nanostructured Materials for the Detection of CBRN* (Springer Netherlands, Dordrecht, 2018), pp. 47–58.
- [43] W. Yao, S. A. Yang, and Q. Niu, Edge States in Graphene: From Gapped Flat-Band to Gapless Chiral Modes, *Phys. Rev. Lett.* **102**, 096801 (2009).
- [44] Y. Ren, Z. Qiao, and Q. Niu, Topological phases in two-dimensional materials: A review, *Rep. Prog. Phys.* **79**, 066501 (2016).
- [45] V. J. Goldman and B. Su, Resonant tunneling in the quantum Hall regime: Measurement of fractional charge, *Science* **267**, 1010 (1995).
- [46] S. M. Mills, A. Gura, K. Watanabe, T. Taniguchi, M. Dawber, D. V. Averin, and X. Du, Dirac fermion quantum Hall antidot in graphene, *Phys. Rev. B* **100**, 245130 (2019).
- [47] F. E. Camino, W. Zhou, and V. J. Goldman, Quantum transport in electron Fabry-Perot interferometers, *Phys. Rev. B* **76**, 155305 (2007).
- [48] C. Gutiérrez, L. Brown, C. J. Kim, J. Park, and A. N. Pasupathy, Klein tunnelling and electron trapping in nanometre-scale graphene quantum dots, *Nat. Phys.* **12**, 1069 (2016).
- [49] P. G. Silvestrov and K. B. Efetov, Quantum Dots in Graphene, *Phys. Rev. Lett.* **98**, 016802 (2007).
- [50] A. Weiße, G. Wellein, A. Alvermann, and H. Fehske, The kernel polynomial method, *Rev. Mod. Phys.* **78**, 275 (2006).
- [51] A. Ferreira and E. R. Mucciolo, Critical Delocalization of Chiral Zero Energy Modes in Graphene, *Phys. Rev. Lett.* **115**, 106601 (2015).
- [52] D. Moldovan, M. Andelković, and F. Peeters, pybinding v0.9.4: A Python package for tight-binding calculations, Zenodo (2017), <https://doi.org/10.5281/zenodo.826942>.
- [53] A. Belayadi, and B. Bourahla, Electronic quantum scattering across molecular junctions: Oligoacenes and oligophenyl graphene strips, *Comput. Condens. Matter* **24**, e00493 (2020).
- [54] A. Belayadi, B. Bourahla, and A. Mougari, An analytical description of the magnetic conductance across an isolated defect region in a 1D-ferromagnetic lead, *Spin* **09**, 1950005 (2019).
- [55] C. W. Groth, M. Wimmer, A. R. Akhmerov, and X. Waintal, Kwant: A software package for quantum transport, *New J. Phys.* **16**, 063065 (2014).
- [56] M. Istas, C. Groth, A. R. Akhmerov, M. Wimmer, and X. Waintal, A general algorithm for computing bound states in infinite tight-binding systems, *SciPost Phys.* **4**, 026 (2018).
- [57] T. Ozaki, K. Nishio, and H. Kino, Efficient implementation of the nonequilibrium Green function method for electronic transport calculations, *Phys. Rev. B* **81**, 035116 (2010).
- [58] W. Ortiz, N. Szpak, and T. Stegmann, Graphene nanoelectromechanical systems as valleytronic devices, *Phys. Rev. B* **106**, 035416 (2022).